Analysis and Suppression of Induced Voltage Pulsation in DC Winding of Five-Phase Wound-Field Switched Flux Machines

Z. Z. Wu, *Member, IEEE*, Z. Q. Zhu, *Fellow, IEEE*, Wei Hua, *Senior Member, IEEE*, Sam Akehurst, Xiaofeng Zhu, Jie Hu, Haoyang Li and Junming Zhu

***Abstract*– In wound-field (WF) switched flux (SF) (WFSF) machines, the DC winding induced voltage pulsation causes current ripple in the DC winding and challenges the DC power source, and deteriorates the control performance. In this paper, the induced voltage pulsation in DC winding of five-phase WFSF machines is analyzed and its reduction methods are proposed. The cycles per electric period of the open-circuit and armature reaction induced voltage pulsation in DC winding are derived analytically. Modifying the airgap permeance by optimizing the rotor pole arc or chamfering the rotor pole surface, and axial pairing of rotor segments having rotor pole with different arcs are used to suppress the induced voltage pulsation in DC winding, with >90% average torque maintained. Finite element results show that, by optimizing the rotor pole arc, the peak-to-peak value of the induced voltage pulsation in DC winding can be effectively suppressed to 59.59%, 30.67%, 29.99% and 43.35% for the 10-stator-pole five-phase WFSF machines with 8-, 9-, 11- and 12-rotor-pole rotors, respectively. By applying rotor pole surface shaping, the induced voltage pulsation in DC winding peak-to-peak value can be effectively suppressed to 61.76%, 45.47% and 40.21% for the 8-, 9- and 12-rotor-pole machines, respectively, while by applying axial pairing, it can be suppressed to 46.89%, 7.16%, 15.64% and 12.04%, respectively. The 10-stator-pole/12-rotor-pole WFSF machines having the original rotor, optimized rotor, chamfered rotor and axial paired rotor are prototyped and the experiments validate the analytical and finite element results.**

***Index Terms*— Five-phase, flux switching, induced voltage pulsation in DC winding, rotor pole arc, rotor pole pairing, rotor pole shaping, switched flux, wound-field.**

I. Introduction

DUE to the high torque/power density and high efficiency, permanent magnet (PM) synchronous machines have been used in many applications [1]-[7]. However, the price and supply of the rare-earth PMs are unstable nowadays [8]. By replacing PMs with DC windings, the wound-field synchronous machine may be a good solution to tackle this challenge [9]-[12]. Compared with the conventional wound-rotor synchronous machines [13] having rotor DC winding, the wound-stator synchronous machines (WSSMs) in which both AC and DC windings are placed in the stator are promising due to the exemption of slips and brushes.

Apart from WSSMs, there are some other types of non-PM machines exempted from the slips and brushes, such as induction machines (IMs) [14], switched reluctance machines (SRMs) [15], [16], and synchronous reluctance machines (SynRMs) [17]. Two recent successful commercial examples include the ABB's SynRMs for industrial applications and the IMs for Tesla electric vehicles. However, IMs suffer from a low efficiency in low-speed/light-load region, which may degrade fuel consumption or system efficiency in hybrid electric vehicles (HEVs) [9]. SRMs have several disadvantages including the high torque ripple and hence noise [12], as well as a nonstandard inverter topology. Compared with the SynRM, the WSSM has a more robust rotor and is more suitable for high speed range of HEVs. Therefore, the WSSM may have the potential for HEVs with several machine prototypes built and tested in [9], [11], [12], and wind power generation [18]-[20].

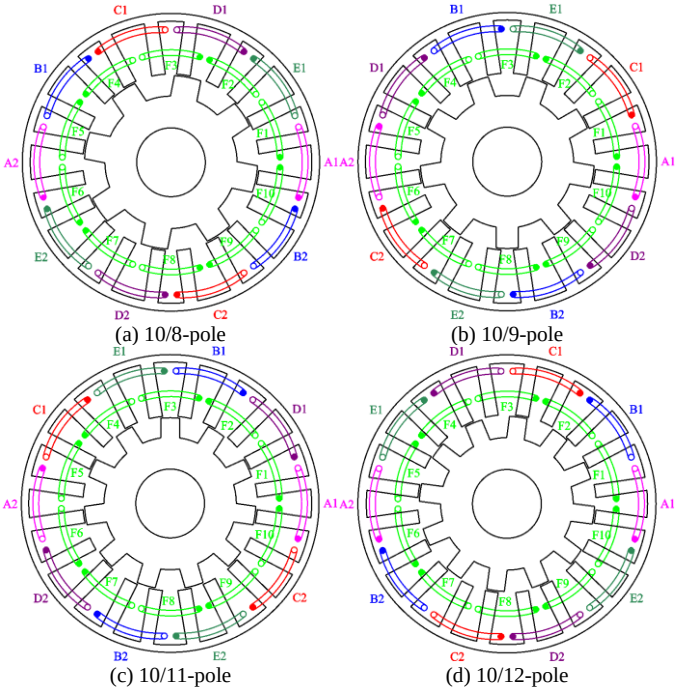

Fig. 1. Cross-sections of four analyzed five-phase 10-stator-pole WFSF machines having 8-, 9-, 11- and 12-rotor-pole rotors.

As a typical wound-stator synchronous machine [18]-[39], single and three-phase wound-field (WF) switched flux (SF) (WFSF) machines are analyzed in [23] and [24], respectively. Various structures of WFSF machines are reviewed and compared in [25]-[27]. In [28], the segmented rotor topology is employed in WFSF machines to achieve a non-overlapping winding topology, despite of the phase back

Manuscript received October 13, 2018; revised March 17, 2019 and July 29, 2019; accepted August 22, 2019. Paper no. TEC-01037-2018. *(Corresponding Author: Z. Q. Zhu.)*

Z. Z. Wu and Sam Akehurst are with Department of Mechanical Engineering, University of Bath, Bath BA2 7AY, U.K. (email: z.wu@bath.ac.uk; s.akehurst@bath.ac.uk).

Z. Q. Zhu is with Department of Electronic and Electrical Engineering, University of Sheffield, Sheffield S10 2TN, U.K. (email: z.q.zhu@sheffield.ac.uk).

Wei Hua, Xiaofeng Zhu, Jie Hu, Haoyang Li and Junming Zhu are with School of Electrical Engineering, Southeast University, Nanjing 210096, China (email: huawei1978@seu.edu.cn; zhuxiaofeng8908@163.com; 220172623@seu.edu.cn; 1175653045@qq.com; 220172748@seu.edu.cn).

EMF even-order harmonics and hence a large torque ripple. In [29], WFSF machines with the non-overlapping winding topology and salient rotors are firstly proposed, in which the adjacent DC coils are of opposite polarities. In [30], a new type of WFSF machines with non-overlapping winding topology and salient rotor is analyzed, however, they have all the DC coils with the same polarity. Another type of WF machines having the non-overlapping winding topology and salient rotors is that having each stator tooth wound by both DC coil and AC coil [12], [31]-[35]. As compared in [25], among these types of the WF machines, the counterpart having overlapping winding topology and salient rotor analyzed in [9]-[11] and [24] exhibits a higher torque density than other types. Five-phase SF machines with both DC winding and PMs are analyzed in [40], which can offer a high fault-tolerant capability [41]-[46] apart from the flux regulation capability.

As shown in TABLE I, compared with the three-phase Toyota Prius 2010 interior PM (IPM) machine [47], [48], the three-phase 12/10-stator/rotor-pole WFSF machines can exhibit a similar torque performance including both average torque T_{avg} and torque ripple T_{rip}, which is defined as the ratio of peak-to-peak torque to the average torque T_{avg}. Due to a larger slot area than the three-phase 12/10-pole WFSF machine, the five-phase 10/12-stator/rotor-pole WFSF machine has a 17.04% higher average torque T_{avg} than the Toyota Prius 2010 IPM machine, i.e. 241.2Nm and 205Nm, respectively, and a much lower torque ripple T_{rip}, i.e. 1.43% and 9.96%, respectively. However, as expected, compared with the efficiency η=90.30% of the Toyota Prius 2010 IPM machine, both the five-phase 10/12-pole and the three-phase 12/10-pole WFSF machines exhibit a slightly lower efficiency, i.e. η=84.18% and η=84.30%, respectively, which is mainly due to the DC winding copper loss. These three machines have the same space envelope, i.e. the stator outer diameter O_{so}=264mm and stack length l_s=50mm, and the same airgap width g=0.73mm, as well as the same rotor inner diameter O_{ri}=51mm. They also have the same slot packing factor k_{pf}=0.465 and the same winding current density J_s=26.8A/mm^2, as well as the lamination stacking factor k_s=0.94. Other main dimensional parameters of the two WFSF machines are listed in TABLE XII in Appendix A.

The WFSF machines can be exempted from the cogging torque, which is suffered by the PM machines. However, the induced voltage pulsation in the DC winding, which increases in direct proportion to the rotor speed, will induce current ripple in the DC winding and challenge the DC power source, and the control performance will also be deteriorated [28], [47], [50]. In [28], it is found that the measured DC winding current ripple is about 19%, which is caused by the induced voltage pulsation in DC winding. In [47], the impact of the DC coil number and the parallel branch number on the induced voltage pulsation in the DC winding is investigated, with some design recommendations for WFSF machines given. In [50], skewing is introduced to minimize the open-circuit induced voltage pulsation in DC winding.

In this paper, the induced voltage pulsation in DC winding of five-phase WFSF machines, e.g. the 10/8-pole counterpart shown in Fig. 1(a), is extended from open-circuit operation condition [50] to on-load operation condition, and some other reduction methods besides skewing [50] are proposed. This paper is arranged as follows. The five-phase WFSF machines are introduced in section II in terms of machine topology and operation principle, as well as feasible combinations of stator pole number and rotor pole number. Then, in section III, the on-load induced voltage pulsation in DC winding is analytically modelled in terms of harmonic orders. This leads to some reduction methods proposed in section IV. Prototypes are built and the experiments validate the analytical and finite element results in section V, followed by conclusions in section VI.

TABLE I
COMPARISON OF WFSF MACHINES AND TOYOTA PRIUS 2010 IPM MACHINE [47], [48] AT RATED CONDITION

Item	Unit	5-Phase WFSF	3-Phase WFSF	IPM
Winding current density, J_s [47]	A/mm^2	26.8	26.8	26.8
Rotor speed, Ω_r [47]	r/min	2795	2795	2795
Average torque, T_{avg} [47]	Nm	241.2	205.2	205
Torque ripple, T_{rip}	%	**1.43**	**7.26**	**9.96**
Average power, P_{avg} [47]	kW	70.6	60	60
AC windings stack copper loss, p_{cuas}	kW	2.40	2.15	2.04
AC windings end copper loss, p_{cuae}	kW	3.85	3.01	4.04
Total AC windings copper loss, p_{cu}	kW	6.25	5.16	6.08
DC winding stack copper loss, p_{cufs}	kW	2.16	2.10	-
DC winding end copper loss, p_{cufe}	kW	3.53	2.92	-
Total copper loss, p_{cu}	kW	11.94	10.17	6.08
Iron loss, p_{iron}	kW	1.12	0.85	0.32
PM eddy current loss, p_{PM}	kW	-	-	0.01
Efficiency, η	%	**84.18**	**84.30**	**90.30**

TABLE II
KEY PARAMETERS OF THE FOUR ANALYSED FIVE-PHASE WFSF MACHINES

Items	10/8	10/9	10/11	10/12	Unit
Stack length, l_s		100			mm
Stator outer radius, R_{so}		45			mm
Rotor inner radius, R_{ri}		10.4			mm
Rotor yoke radius, R_{ry}		20			mm
Airgap length, g		0.5			mm
Stator yoke radius, R_{sy}	42.6	42.7	42.8	42.5	mm
Stator inner radius, R_{si}	26.7	26.7	26.4	26.9	mm
Arc of stator tooth, θ_{st}	8.9	9.0	8.9	8.4	°
Arc of stator slot for DC coils, θ_{ssdc}	10.8	10.2	8.2	8.1	°
Arc of rotor pole, θ_{rp}	17.9	14.6	12.6	11.6	°
Stack copper loss of DC winding, p_{cuf}		60			W
DC winding slot filling factor, k_{pff}		0.5			-
DC coil number of turns, N_{fc}		90			-
Current in DC winding, I_f	2.56	2.51	2.32	2.22	A
DC winding resistance voltage drop, V_R	23.44	23.90	25.86	27.03	V
Stack copper loss of AC windings, p_{cua}		60			W
AC windings slot filling factor, k_{pfa}		0.5			-
AC coil number of turns, N_{ac}		36			-
RMS current in AC windings, I_{RMS}	5.47	5.66	6.31	6.37	A

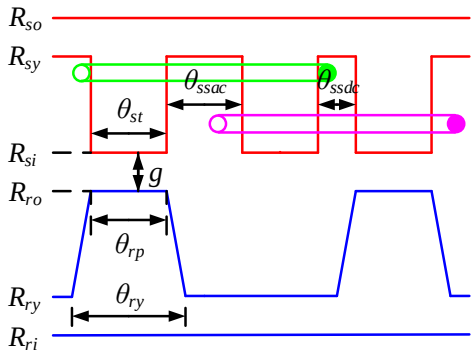

Fig. 2. Linear illustration of dimensional parameters for WFSF machines.

II. FIVE-PHASE WFSF MACHINES

A. Machine Topology and Operation Principle

As compared in [25], the three-phase WFSF machine having an overlapping winding topology and salient rotor analyzed in [9]-[11] and [24] exhibits a higher torque density

than other types of WFSF machines. Thus, the five-phase WFSF machines have an overlapping winding topology as those in [9]-[11] and [24] are chosen to be analyzed in this paper, as shown in Fig. 1(a) for the 10/8-pole counterpart. Both AC and DC windings are accommodated in the stator in WFSF machines, whilst the rotor is the same as that of switched reluctance machines [15], [16]. The DC winding consists of several DC coils connected in series, whilst each AC phase winding is also made up of several AC coils connected in series. Similar to the SFPM machines, the operation principle of WFSF machines can be explained by the magnetic gearing effect [51]-[53]. Both the static open-circuit MMF and the rotating armature reaction MMF due to AC and DC windings, respectively, are modulated by the salient rotor, resulting in pairs of synchronized airgap field harmonics and generated airgap electromagnetic torque.

B. Feasible Stator/Rotor-Pole Combinations

There are plenty of airgap flux density harmonics in WFSF machines including those generating coil back EMF even-order harmonics, caused by rotor saliency and magnetic gearing effect [30]-[32]. However, as well known, the conventional rotor-excitation machines are exempt from the even-order back EMF harmonics. To possibly eliminate the even-order harmonics in the back EMF of the phase winding and hence reduce the torque ripple pulsation, the armature coil number per phase N_{spp} in WFSF machines is desired as an even number $2k$ (k=1,2,3,…),

$$N_{spp} = \frac{N_s}{m} = 2k \tag{1}$$

where N_s is the number of stator poles. m is the number of phases.

Based on (1), in the analyzed five-phase WFSF machines, i.e. m=5, the stator pole number N_s=10k. The pitch factor k_{pv} for the v^{th} back EMF harmonic in the N_s/N_r-pole WFSF machine can be given by,

$$k_{pv} = \left|\cos\left[v\pi\left(\frac{N_r}{N_s} - 1\right)\right]\right| \tag{2}$$

where N_r is the number of rotor poles.

Based on (2), to achieve a larger average electromagnetic torque, the rotor pole number N_r is designed as N_r=N_s±2 or N_r=N_s±1 with a larger fundamental pitch factor obtained, despite the latter ones suffering from the unbalanced magnetic pull.

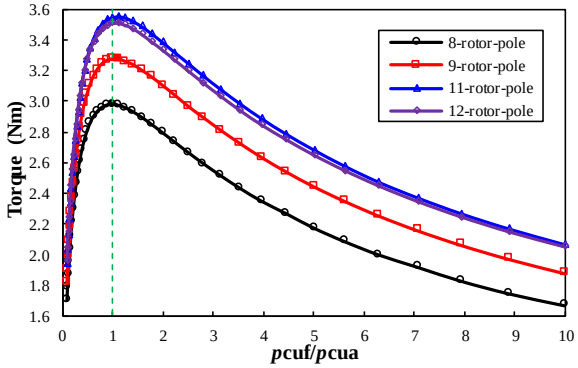

Fig. 3. Influence of copper loss ratio on average electromagnetic torque (p_{cu}=120W, BLAC, i_d=0).

In this paper, the five-phase WFSF machines with k=1, i.e. N_s=10, having N_r=8, 9, 11 and 12 will be analyzed. TABLE II lists their dimensional parameters. The parameters from stack length l_s to airgap length g are fixed, whilst those from stator yoke radius R_{sy} to rotor pole arc θ_{rp} are globally optimized by genetic algorithm for the largest average electromagnetic torque, with the total stack copper loss set as 120W. When the stack copper loss of DC winding p_{cuf} and that of AC windings p_{cua} are equal, the average electromagnetic torque will be the maximum [24]. This can be verified by the FE predicted variation of average electromagnetic torque with copper loss ratio in Fig. 3, in which the magnetic saturation is considered and the copper loss ratio is defined as the ratio of p_{cuf} to p_{cua}. As shown in Fig. 3, the maximum electromagnetic torque can be achieved when p_{cuf}/p_{cua}=1 in all the four analyzed WFSF machines having optimized dimensional parameters shown in TABLE II. Therefore, in this paper all the four analyzed WFSF machines have p_{cua}=p_{cuf}=60W. Moreover, they all operate under zero d-axis armature current control, i.e. i_d=0, at BLAC mode, since the d- and q-axis inductances are similar and hence the reluctance torque is negligible [53]. The dimensional parameters shown in TABLE II can be referred in Fig. 2, in which R_{ro} and θ_{ssac} are outer radius of rotor and arc of stator slot for AC coils, respectively.

TABLE III
DISTRIBUTION FACTORS FOR FIVE-PHASE WFSF MACHINES (r=1,2,3…)

Harmonic order	10/8	10/9	10/11	10/12
2r-1	1	1	1	1
2r	1	0	0	1

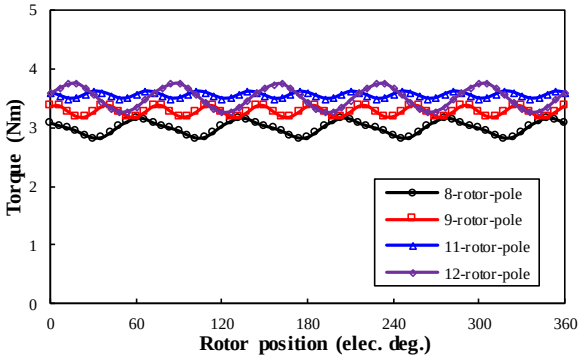

Fig. 4. Rated on-load torque waveforms in the four analyzed WFSF machines (p_{cuf}=60W, p_{cua}=60W, BLAC, i_d=0).

The winding factor k_v for the v^{th} back EMF harmonic in the N_s/N_r-pole WFSF machine can be given by,

$$k_v = k_{pv}k_{dv} \tag{3}$$

where k_{dv} is the v^{th} back EMF harmonic distribution factor.

Based on the pitch and distribution factors shown in (2) and TABLE III, respectively, the winding factor k_v for the four analyzed five-phase WFSF machines can be obtained. Obviously, the even-order harmonic winding factors in the machines having 9- and 11-rotor-pole rotors are zero whilst those in the machines having 8- and 12-rotor-pole rotors are non-zero, as evidenced by torque waveforms in Fig. 4. In Fig. 4, the torque ripples T_{rip} are 11.43%, 5.50%, 3.50% and 14.36% for 10/8-, 10/9-, 10/11- and 10/12-pole WFSF machines, respectively. Here, T_{rip} is defined as,

$$T_{rip} = \frac{T_{max} - T_{min}}{T_{avg}} \times 100\% \tag{4}$$

where T_{max}, T_{min} and T_{avg} are the maximum, minimum and average electromagnetic torques, respectively.

C. Losses and Efficiency

The losses and efficiency of the four analyzed five-phase WFSF machines are given in TABLE IV. The iron loss p_{fe} in TABLE IV is given by,

$$\begin{aligned} p_{fe} &= p_h + p_e + p_x \\ &= k_h f B_m^2 + k_e f^2 B_m^2 + k_x f^{1.5} B_m^{1.5} \end{aligned} \tag{5}$$

where p_h, p_e and p_x are the hysteresis loss, eddy current loss and excess loss, respectively, whilst k_h, k_e and k_x are the

coefficients for these three components, respectively. Here, k_h=214.91W/m^3 and k_e=0.33W/m^3 for M270-35A lamination steel, whilst k_x is neglected, i.e. k_x=0. f and B_m are the electric frequency and the maximum flux density, respectively.

As shown in TABLE IV, the iron loss p_{fe} is much smaller than the copper loss p_{cu} due to a low rotor speed 400rpm. Hence, only the copper loss is taken into consideration in the foregoing machine optimization, whilst the iron loss is not taken into consideration. It is worth noting that single-side end-winding length for each DC coil L_{ef} is calculated by [54],

$$L_{ef} = K_s \tau_f + 2d_1 = K_s \frac{R_{sy} + R_{si}}{2}\left(\theta_{sp} - \frac{\theta_{ssdc}}{2}\right) + 2d_1 \quad (6)$$

where K_s is the end-winding shape empirical coefficient, which is set as 1.3 for the analyzed five-phase 10-stator-pole WFSF machines [54]. τ_f is the DC coil pitch circumferential length. d_1 is the length of the straight part of the end-winding, which is set as 5mm. θ_{sp} is the stator pole pitch, i.e. $2\pi/N_s$. θ_{ssdc} is the arc of stator slot for DC coils listed in TABLE II.

Based on (6), the end-winding copper loss of DC winding p_{cufe} can be obtained, as shown in TABLE IV. Similarly, that of AC windings p_{cuae} can also be obtained, as shown in TABLE IV. As shown in TABLE IV, all the four analyzed WFSF machines have similar total copper loss p_{cu}. As for efficiency η, the 10/11- and 10/8-pole WFSF machines have the highest and lowest efficiencies due to the highest and lowest average electromagnetic torques shown in Fig. 4. The efficiency η shown in TABLE IV is defined as,

$$\eta = \frac{P_o}{P_i} \times 100\% = \frac{P_{em} - p_{fe}}{P_{em} + p_{cu}} \times 100\% \quad (7)$$

where P_o and P_i are the output and input powers, respectively. P_{em} is the electromagnetic power.

TABLE IV
LOSSES AND EFFICIENCY OF FIVE-PHASE WFSF MACHINES AT 400RPM

Items	Unit	10/8	10/9	10/11	10/12
Iron loss, p_{fe}	W	2.46	2.60	3.73	4.46
Stack copper loss of DC winding, p_{cuf}	W	60	60	60	60
End-winding copper loss of DC winding, p_{cufe}	W	17.94	18.12	18.55	18.62
Stack copper loss of AC windings, p_{cua}	W	60	60	60	60
End-winding copper loss of AC windings, p_{cuae}	W	18.78	18.67	18.10	17.87
Total copper loss, p_{cu}	W	156.72	156.80	156.64	156.49
Electromagnetic torque, T_{em}	Nm	2.98	3.27	3.55	3.51
Electromagnetic power, P_{em}	W	125.01	137.17	148.68	146.91
Output power, P_o	W	122.56	134.57	144.96	142.46
Input power, P_i	W	281.73	293.96	305.33	303.40
Efficiency, η	%	43.50	45.78	47.48	46.95

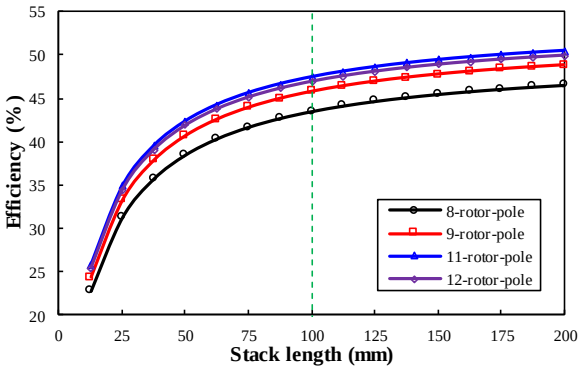

Fig. 5. Variation of efficiency with stack length in the four analyzed five-phase WFSF machines (p_{cuf}=p_{cua}, BLAC, i_d=0).

When the magnetic field of the WFSF machine is kept the same, the stack copper losses of DC winding p_{cuf} and AC windings p_{cua} will be proportional to the stack length l_s, as well as the iron loss p_{fe} and the electromagnetic power P_{em}. However, both the end-winding copper loss of DC winding p_{cufe} and that of AC windings p_{cuae} will remain the same. Therefore, the efficiency η will be reduced if a shorter stack is chosen, as shown in Fig. 5. However, as the ratio of end-winding copper loss to the total copper loss is smaller when the stack length is longer, the variation of efficiency with stack length becomes saturated for a longer stack, as evidenced by Fig. 5.

III. ON-LOAD INDUCED VOLTAGE PULSATION IN DC WINDING

When saturation in the lamination steel is neglected, the on-load induced voltage pulsation in DC winding v_{load} can be obtained by,

$$v_{load}(\theta_e) = v_{open}(\theta_e) + v_{arma}(\theta_e) \quad (8)$$

where v_{open} and v_{arma} are the open-circuit and armature reaction induced voltage pulsations in DC winding, respectively.

When the DC coils in WFSF machines are in the series connection, the open-circuit induced voltage pulsation in DC winding v_{open} can be given by [50],

$$v_{open} = \sum_{i=0,1,2,\ldots}^{\infty} \psi_i i N_r \Omega_m \frac{\sin N_r i\pi}{\sin \frac{N_r i}{N_s}\pi} \cos\left(N_r i\theta_m + N_r i\pi - \frac{N_r i}{N_s}\pi + \theta_i\right) \quad (9)$$

where θ_i and ψ_i (i=1,2,3…) are the i^{th} flux-linkage harmonic initial phase and amplitude of DC coil 1, respectively. Ω_m is the rotor mechanical speed.

As for the cycles per electric period of the open-circuit induced voltage pulsation in DC winding N_{peopen}, it can be given by [50],

$$N_{peopen} = \frac{LCM(N_s, N_r)}{N_r} \quad (10)$$

The armature reaction DC winding flux-linkage ψ_{arma} can be given by,

$$\psi_{arma}(\theta_e) = \sum_{k=1,2,3,4,5} \psi_{armak}(\theta_e) \quad (11)$$

where ψ_{armak} with k=1, 2, 3, 4 and 5 are the armature reaction DC winding flux-linkage due to A-, B-, C-, D- and E-phase currents, respectively, which are given by,

$$\psi_{armak}(\theta_e) = M_{fk}(\theta_e) \times I_k(\theta_e) \quad (12)$$

where M_{fk} with k=1, 2, 3, 4 and 5 are the mutual inductances between the DC winding and the A-, B-, C-, D- and E-phase windings, respectively, which can be given by,

$$M_{fk}(\theta_e) = \sum_{j=1,2,3,\ldots}^{\infty} k_{pj} k_{dj} M_j \cos\left\{j\left[\theta_e - \frac{2(k-1)}{5}\pi\right] + \alpha_j\right\} \quad (13)$$

where $k_{pj}k_{dj}M_j$ is the j^{th} mutual inductance harmonic amplitude. α_j is the M_{f1} j^{th} harmonic initial phase.

In (12), I_k with k=1, 2, 3, 4 and 5 are the the A-, B-, C-, D- and E-phase currents, respectively. When five-phase symmetrical sinusoidal currents are injected, I_k can be given by,

$$I_k(\theta_e) = I_{arma} \cos\left[\theta_e - \frac{2(k-1)}{5}\pi + \beta_1\right] \quad (14)$$

where I_{arma} is the fundamental amplitude. β_1-2(k-1)π/5 is the initial phase. β_1 is the initial phase for A-phase current.

Submitting (12), (13) and (14) into (11), ψ_{arma} in the five-phase WFSF machine can be rewritten as,

$$\psi_{arma}(\theta_e) = \sum_{j=1,2,3,\dots}^{\infty} k_{pj}k_{dj}M_j I_{arma}(p_1 \cos a \cos b + p_2 \sin a \sin b) \quad (15)$$

where

$$\begin{cases} a = j\theta_e + \alpha_j \\ b = \theta_e + \beta_1 \end{cases} \quad (16)$$

and

$$\begin{cases} p_1 = 1 + 2\cos\frac{2j\pi}{5}\cos\frac{2\pi}{5} + 2\cos\frac{4j\pi}{5}\cos\frac{4\pi}{5} \\ p_2 = 2\sin\frac{2j\pi}{5}\sin\frac{2\pi}{5} + 2\sin\frac{4j\pi}{5}\sin\frac{4\pi}{5} \end{cases} \quad (17)$$

The coefficients p_1 and p_2 in (17) can be calculated as TABLE V. Therefore, ψ_{arma} in (15) can be simplified as,

$$\psi_{arma}(\theta_e) = \sum_{j=1,2,3,\dots}^{\infty} \frac{5}{2}k_{pj}k_{dj}M_j I_{arma} \times \begin{cases} \cos[(j-1)\theta_e + \alpha_j - \beta_1], when\ \ j = 5r-4 \\ \cos[(j+1)\theta_e + \alpha_j + \beta_1], when\ \ j = 5r-1 \\ 0 \qquad\qquad\qquad\qquad , otherwise \end{cases} \quad (18)$$

The armature reaction induced voltage pulsation in DC winding v_{arma} in five-phase WFSF machines can be obtained as,

$$v_{arma}(\theta_e) = \frac{d\psi_{arma}}{dt} = \omega_e \frac{d\psi_{arma}}{d\theta_e} \quad (19)$$

Submitting (18) into (19), v_{arma} can be rewritten by,

$$v_{arma}(\theta_e) = \sum_{j=1,2,3,\dots}^{\infty} \frac{5}{2}\omega_e k_{pj}k_{dj}M_j I_{arma} \times \begin{cases} -(j-1)\sin[(j-1)\theta_e + \alpha_j - \beta_1], when\ \ j = 5r-4 \\ -(j+1)\sin[(j+1)\theta_e + \alpha_j + \beta_1], when\ \ j = 5r-1 \\ 0 \qquad\qquad\qquad\qquad\ , otherwise \end{cases} \quad (20)$$

As shown in (20), the armature reaction induced voltage pulsation in DC winding v_{arma} in five-phase WFSF machines are with $(5r)^{th}$ harmonics when the corresponding harmonic winding factor is non-zero. Since the even-order harmonics in the 10/9- and 10/11-pole WFSF machines are zero whilst those in the 10/8- and 10/12-pole counterparts are non-zero, the armature reaction induced voltage pulsation in DC winding cycles per electric period N_{pearma} is 5, 10, 10 and 5 for 10/8-, 10/9-, 10/11- and 10/12-pole WFSF machines, respectively, as shown in TABLE VI. As N_{pearma} and N_{peopen} are the same for each machine, respectively, the resulted on-load induced voltage pulsation in DC winding cycles per electric period N_{peload} is also 5, 10, 10 and 5, respectively. This is verified by the FE predicted results in Fig. 6.

TABLE V
COEFFICIENTS p_1 AND p_2 WITH DIFFERENT j (r=1,2,1…)

j	j	p_1	p_2
5r-4	1, 6, 10, …	2.5	2.5
5r-3	2, 7, 11, …	0	0
5r-2	3, 8, 12, …	0	0
5r-1	4, 9, 13, …	2.5	-2.5
5r	5, 10, 15, …	0	0

TABLE VI
ANALYTICAL PREDICTION OF N_{peopen}, N_{pearma} AND N_{peload}

Item	10-stator-pole WFSF Machines			
N_r	8	9	11	12
N_{peopen}	5	10	10	5
N_{pearma}	5	10	10	5
N_{peload}	5	10	10	5

As shown in TABLE VII, the peak-to-peak value of the on-load induced voltage pulsation in DC winding E_{pp} for the 10/12-pole WFSF machine at 400rpm is 14.99V. This means the ratio of E_{pp} to the DC winding resistance voltage drop V_R is IVR=55.46%, which is proportional to the rotor speed, challenging the DC power source and deteriorate the control performance.

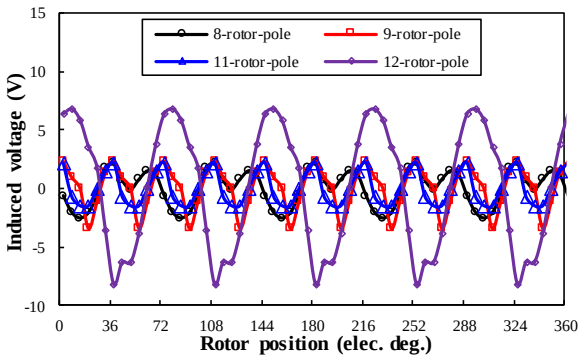

(a) Waveforms

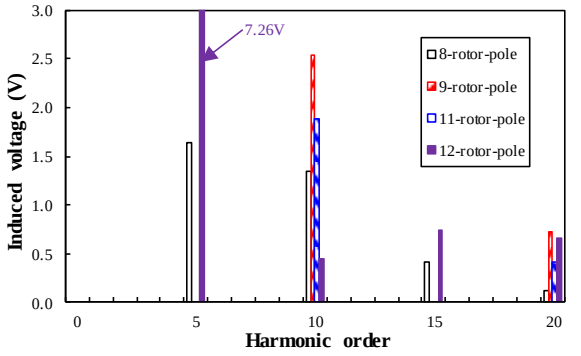

(b) Spectra

Fig. 6. On-load induced voltage in DC windings in the 10-stator-pole five-phase WFSF machines at 400rpm (p_{cuf}=60W, p_{cua}=60W, BLAC, i_d=0).

TABLE VII
CHARACTERISTICS OF INDUCED VOLTAGE PULSATION IN DC WINDINGS, TORQUE AND EFFICIENCY @400RPM

Technique	Item	Unit	10-stator-pole WFSF machines			
-	N_r	-	8	9	11	12
Original	V_R	V	23.44	23.90	25.86	27.03
	E_{pp}	V	4.68	5.82	3.63	14.99
	IVR	%	19.98	24.36	14.02	55.46
	T_{avg}	Nm	2.98	3.27	3.55	3.51
	η	%	43.50	45.78	47.48	46.95
	T_{rip}	%	11.43	5.50	3.50	14.36
θ_{rp} optimization	RT_{avg}	%	99.40	93.18	93.91	98.25
	RE_{pp}	%	59.59	30.67	29.99	43.35
	η	%	43.37	44.14	46.07	46.61
	T_{rip}	%	13.48	5.14	3.89	17.00
Chamfering	RT_{avg}	%	95.64	93.45	97.46	92.07
	RE_{pp}	%	61.76	45.47	93.62	40.21
	η	%	42.44	44.16	46.34	46.65
	T_{rip}	%	6.78	3.00	2.68	6.97
Pairing	RT_{avg}	%	90.99*	90.65	93.55	90.82
	RE_{pp}	%	46.89*	7.16	15.64	12.04
	η	%	41.24*	43.48	45.98	44.73
	T_{rip}	%	2.93*	2.34	2.41	7.18

*: These two values are based on 3-segment axial pairing. As for 2-segment axial pairing, RT_{avg}=99.06%, RE_{pp}=52.65%, η=43.27% and T_{rip}=12.19%, respectively.

IV. SUPPRESSION OF INDUCED VOLTAGE PULSATION IN DC WINDING BY MODIFYING AIRGAP PERMEANCE

The on-load airgap flux density B_{load} will produce an on-load flux-linkage ψ_{fk} in the DC coil f_k (k=1,2,3,…,N_s),

$$\psi_{fk}(\theta_e) = (-1)^{k+1}\int_{(k-1)\theta_{stp}+\frac{\theta_{sdc}}{2}}^{k\theta_{stp}-\frac{\theta_{sdc}}{2}} B_{load}(\theta_e, \delta)\, d\delta \quad (21)$$

where θ_{stp} is stator tooth pitch arc. δ is airgap mechanical

position.

If saturation in the lamination steel is neglected, the on-load airgap flux density B_{load} can be given by,

$$B_{load}(\theta_e, \delta) = B_{open}(\theta_e, \delta) + B_{arma}(\theta_e, \delta) \quad (22)$$

where B_{open} is open-circuit airgap flux density. B_{arma} is armature reaction airgap flux density. They are given by [51],

$$\begin{cases} B_{open}(\theta_e, \delta) = F_{open}(\delta)\Lambda_{ag}(\theta_e, \delta) \\ B_{arma}(\theta_e, \delta) = F_{arma}(\theta_e, \delta)\Lambda_{ag}(\theta_e, \delta) \end{cases} \quad (23)$$

where F_{open} is the open-circuit airgap MMF due to DC winding field excitation, which is static and not relevant to the rotor electric position θ_e. Λ_{ag} is the airgap permeance which is determined by both rotor electric position θ_e and the airgap mechanical position δ. F_{arma} is the armature reaction airgap MMF due to armature reactions.

As can be seen from (21), the m^{th} harmonic of ψ_{fk} is caused by the m^{th} time harmonics of the on-load airgap flux density B_{load}, and hence the m^{th} time harmonics of B_{open} and B_{arma}, based on (22).

As shown in (23), the m^{th} time harmonics of B_{open} should be resulted from the m^{th} time harmonics of Λ_{ag} and hence essentially the m^{th} spatial harmonics of Λ_{ag}, since F_{open} is time-invariant. However, the m^{th} time harmonics of B_{arma} can be originated from either the MMF F_{arma} or the permeance Λ_{ag}, since both are functions of the rotor electric position θ_e. Moreover, modifying the airgap permeance Λ_{ag} can potentially result in a reduction of harmonics of B_{open} and B_{arma} and hence the harmonics in B_{load} and the DC winding flux-linkage and induce voltage.

A. Rotor Pole Arc Optimization

An apparent approach to modify the airgap permeance is optimizing the rotor pole arc θ_{rp}, which is usually conducted in the switched flux PM machine for a more sinusoidal AC windings phase back EMF [55]. As evidenced by Fig. 7, when the criterion that the average electromagnetic torque T_{avg} should be maintained more than 90% is applied, i.e. RT_{avg}>90%, the on-load induced voltage pulsation in DC winding peak-to-peak value E_{PP} is suppressed to RE_{PP}=59.59%, 30.67%, 29.99% and 43.35%, respectively, by selecting the optimal rotor pole arc θ_{rpopt}=17°, 11°, 9° and 10° for the analyzed five-phase 10/8-pole, 10/9-pole, 10/11-pole and 10/12-pole WFSF machines, respectively. However, the torque ripple T_{rip} is slightly increased, i.e. T_{rip}=13.48%, 5.14%, 3.89% and 17.00%, respectively, as shown in Fig. 8 and TABLE VII. It is worth noting that RT_{avg} and RE_{PP} are defined as the ratios of T_{avg} and E_{PP} in the WFSF machine with optimized rotor pole arc to that of its original counterpart, respectively.

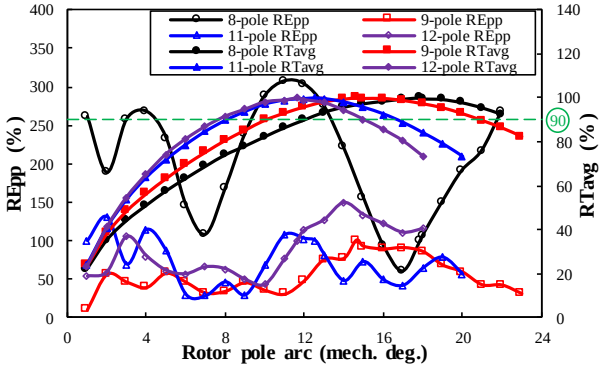

Fig. 7. Influence of rotor pole arc θ_{rp} on RE_{pp} and RT_{avg} at 400rpm (p_{cuf}=60W, p_{cua}=60W, BLAC, i_d=0).

Since the average electromagnetic torque T_{avg} is smaller, the efficiency η of each WFSF machine having the optimal rotor pole arc θ_{rpopt} is also lower than its original counterpart, as shown in TABLE IV and TABLE VIII. As shown in TABLE VII, by applying the rotor pole arc optimization, the efficiency η can be maintained as 43.37%, 44.14%, 46.07% and 46.61% for the analyzed five-phase 10/8-pole, 10/9-pole, 10/11-pole and 10/12-pole WFSF machines, respectively. This is mainly caused by the slightly reduced average electromagnetic torque T_{avg}, as the copper loss is kept the same whilst the iron loss is remained similar but much lower than the copper loss.

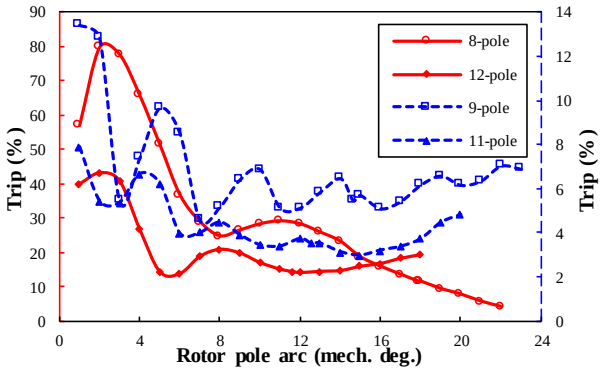

Fig. 8. Influence of rotor pole arc θ_{rp} on T_{rip} at 400rpm (p_{cuf}=60W, p_{cua}=60W, BLAC, i_d=0).

TABLE VIII
LOSSES AND EFFICIENCY OF FIVE-PHASE WFSF MACHINES WITH OPTIMIZED ROTOR POLE ARCS AT 400RPM

Items	Unit	10/8	10/9	10/11	10/12
Iron loss, p_{fe}	W	2.39	2.19	3.14	4.12
Total copper loss, p_{cu}	W	156.72	156.80	156.64	156.49
Electromagnetic torque, T_{em}	Nm	2.97	3.05	3.33	3.45
Efficiency, η	%	43.37	44.14	46.07	46.61

It is worth noting that the criterion of the torque ripple can also be considered, which is important for some applications including wind power generation [18], together with that of the average electromagnetic torque. The corresponding analysis can be referred in Appendix B.

B. Rotor Pole Chamfering

Rotor pole chamfering can also modify the equivalent airgap length and hence the airgap permeance, which is also a typical method used in PM machines to suppress cogging torque [56]. Here, the rotor pole chamfering is conducted as illustrated in Fig. 9, in which the filled area in the original rotor shown in Fig. 1 will be removed in the chamfered rotor. After chamfering, the rotor pole surface center is moved in the radial direction from O to O' with a displacement $d_{OO'}$. It is worth noting that the smallest airgap width in the chamfered rotor should be the same as the airgap width of the original rotor in Fig. 1, which is essential for a fair comparison.

When the criterion that the average electromagnetic torque should be maintained more than 90% is applied, the ratio RE_{PP} will be suppressed to 61.76%, 45.47%, 93.62% and 40.21%, respectively, as shown in Fig. 10, when $d_{OO'}$=6mm, 11mm, 7mm and 15mm for the analyzed five-phase 10/8-pole, 10/9-pole, 10/11-pole and 10/12-pole WFSF machines, respectively. Meanwhile, the average electromagnetic torque T_{avg} can be maintained as 95.64%, 93.45%, 97.46% and 92.07%, respectively. Similar to the cogging torque reduction in [56], as shown in Fig. 11 and TABLE VII, the torque ripple T_{rip} can also be reduced by applying the rotor pole chamfering, i.e. T_{rip}=6.78%, 3.00%, 2.68% and 6.97% for the analyzed five-phase 10/8-pole, 10/9-pole, 10/11-pole and 10/12-pole WFSF machines, respectively.

As shown in TABLE VII, by applying the rotor pole chamfering, the efficiency η can be maintained as 42.44%, 44.16%, 46.34% and 46.65% for the analyzed five-phase 10/8-pole, 10/9-pole, 10/11-pole and 10/12-pole WFSF machines, respectively. Again, this is mainly due to the reduced average electromagnetic torque T_{avg} in the WFSF machines with chamfered rotor poles, as shown in TABLE IX.

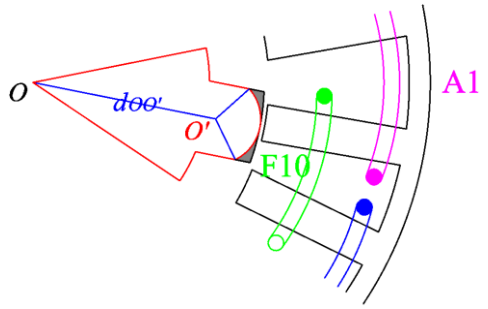

Fig. 9. Illustration of rotor pole chamfering with filled area removed ($d_{OO'}$>0).

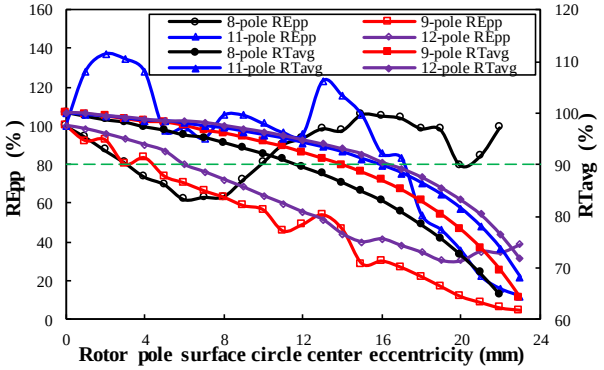

Fig. 10. Influence of rotor pole surface center displacement $d_{OO'}$ on RE_{pp} and RT_{avg} at 400rpm (p_{cuf}=60W, p_{cua}=60W, BLAC, i_d=0).

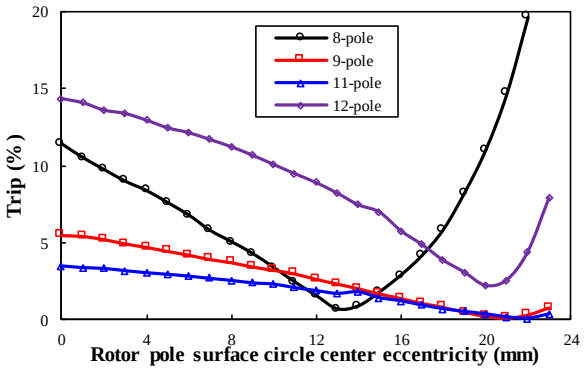

Fig. 11. Influence of rotor pole surface center displacement $d_{OO'}$ on T_{rip} at 400rpm (p_{cuf}=60W, p_{cua}=60W, BLAC, i_d=0).

TABLE IX
LOSSES AND EFFICIENCY OF FIVE-PHASE WFSF MACHINES WITH CHAMFERED ROTOR POLE AT 400RPM

Items	Unit	10/8	10/9	10/11	10/12
Iron loss, p_{fe}	W	2.30	2.34	3.74	3.99
Total copper loss, p_{cu}	W	156.72	156.80	156.64	156.49
Electromagnetic torque, T_{em}	Nm	2.85	3.06	3.40	3.45
Efficiency, η	%	42.44	44.16	46.34	46.65

V. SUPPRESSION OF INDUCED VOLTAGE PULSATION IN DC WINDING BY ROTOR POLE ARC AXIAL PAIRING

From Fig. 7, since the rotor pole arc effectively influences the on-load induced voltage pulsation in DC winding, rotor pole axial pairing [57] can also be adopted to suppress it.

As illustrated in Fig. 12, the axial pairing approach for the 10/8-pole WFSF machine have two segments axially paired, i.e. N_{sg}=2. The principle of the reduction of the on-load induced voltage pulsation in DC winding is described below.

By way of example of the 10/8-pole WFSF machine, the on-load induced voltage pulsation in DC winding v_{load} is given in Fourier series by,

$$v_{load}(\theta_e) = \sum_{i=5,10,15,\dots}^{\infty} v_i = \sum_{i=5,10,15,\dots}^{\infty} v_{loadi}\cos(i\theta_e - \theta_{loadi}) \tag{24}$$

where v_i is the i^{th} harmonic of v_{load}. v_{loadi} and θ_{loadi} are the amplitude and initial phase angle of the i^{th} harmonic, respectively.

For the WFSF sub-machine having rotor pole arc θ_{rpk} (k=1,2,3,…,N_{sg}), the i^{th} harmonic of the on-load induced voltage pulsation in DC winding v_{ik} is given by,

$$v_{ik} = v_{loadik}\cos(i\theta_e - \theta_{loadik}) \tag{25}$$

where θ_{loadik} and v_{loadik} are initial phase angle and the amplitude of the i^{th} harmonic for WFSF machine having rotor pole arc θ_{rpk} (k=1,2,3…), respectively.

When axial flux leakage is neglected, the on-load induced voltage pulsation in DC winding in the WFSF machine having paired rotor v_{loadp} can be given by,

$$v_{loadp}(\theta_e) = \frac{1}{N_{sp}}\sum_{k=1,2,3,\dots}^{N_{sp}}\sum_{i=5,10,15,\dots}^{\infty} v_{ik} = \sum_{k=1,2,3,\dots}^{N_{sp}}\sum_{i=5,10,15,\dots}^{\infty} v_{loadik}\cos(i\theta_e - \theta_{loadik}) \tag{26}$$

As shown in (26), the on-load induced voltage pulsation in DC winding v_{loadp} can be smaller than that of its counterpart with the original rotor. For example, if N_{sg}=2, v_{loadi1}=v_{loadi2} and θ_{loadi2}=θ_{loadi1}+π, the i^{th} harmonic of v_{loadp}, i.e. v_{ip}, can be suppressed to 0, as evidenced by (27).

$$\begin{aligned} v_{ip}(\theta_e) &= \frac{1}{2}[v_{loadi1}\cos(i\theta_e - \theta_{loadi1}) + v_{loadi2}\cos(i\theta_e - \theta_{loadi2})] \\ &= \frac{v_{loadi1}}{2}[\cos(i\theta_e - \theta_{loadi1}) + \cos(i\theta_e - \theta_{loadi1} - \pi)] \\ &= 0 \end{aligned} \tag{27}$$

As shown in Fig. 13, 2-segment axial pairing can effectively suppress the on-load induced voltage pulsation in DC winding by selecting the appropriate combination of θ_{rp1} and θ_{rp2}. However, as shown in Fig. 14, this may cause a larger reduction in the average electromagnetic torque T_{avg}, i.e. a smaller RT_{avg}.

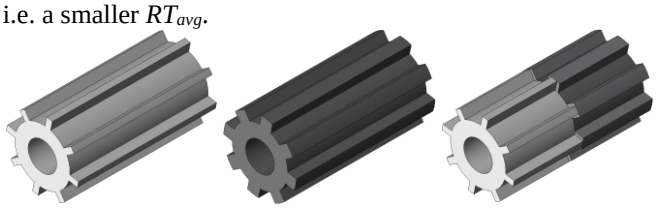

(a) θ_{rp1} (b) θ_{rp2} (c) Paired of θ_{rp1} and θ_{rp2}

Fig. 12. Illustration of rotor axial pairing with N_{sg}=2.

As shown from Fig. 16 to Fig. 19, when the criterion that T_{avg} should be maintained more than 90% is applied, i.e. R_{Tavg}>90%, the on-load induced voltage pulsation in DC winding can be suppressed to RE_{PP}=52.65%, 7.16%, 15.64% and 12.04%, respectively, by choosing (θ_{rp1}, θ_{rp2}) as (16°, 18°), (9°, 12°), (8°, 10°) and (6°, 11°) for the analyzed five-phase 10/8-pole, 10/9-pole, 10/11-pole and 10/12-pole WFSF machines, respectively. Meanwhile, the average electromagnetic torque can also be maintained as R_{Tavg}=99.06%, 90.65%, 93.55% and 90.82%, respectively. As shown in Fig. 15 and TABLE VII, when applying the

rotor pole axial pairing, the torque ripple T_{rip} can be reduced in the 10/9-, 10/11- and 10/13-pole WFSF machines, i.e. T_{rip}=2.34%, 2.41% and 7.18%. However, it will be slightly higher in the 10/8-pole WFSF machine, i.e. T_{rip}=12.19%.

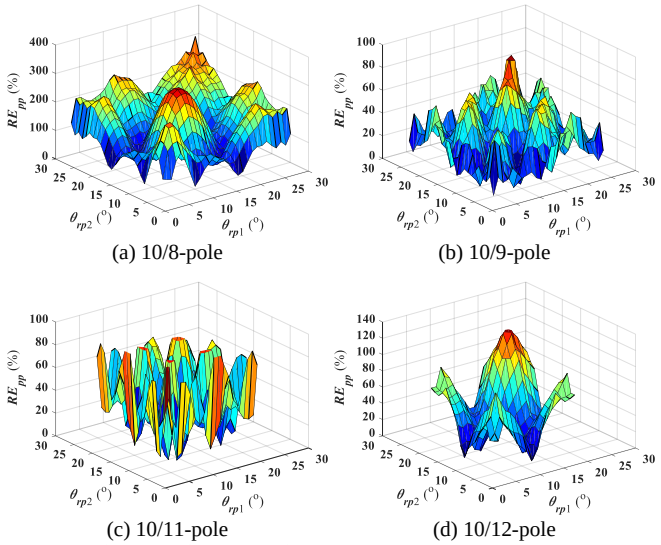

(a) 10/8-pole (b) 10/9-pole

(c) 10/11-pole (d) 10/12-pole

Fig. 13. Influence of θ_{rp1} and θ_{rp2} on RE_{pp} at 400rpm (N_{sg}=2, p_{cuf}=60W, p_{cua}=60W, BLAC, i_d=0).

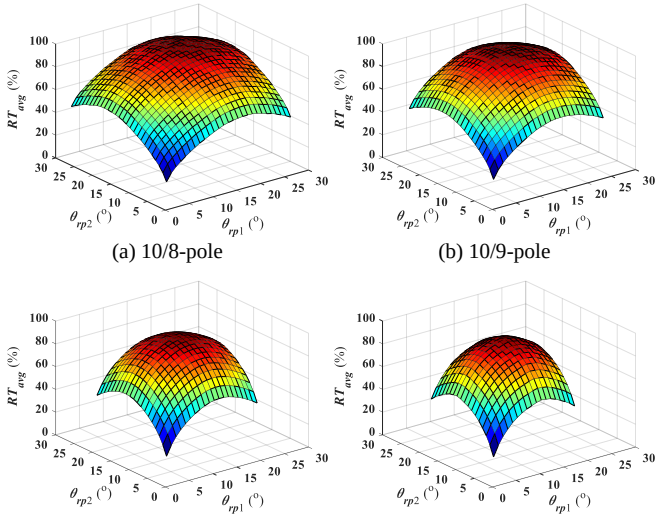

(a) 10/8-pole (b) 10/9-pole

(c) 10/11-pole (d) 10/12-pole

Fig. 14. Influence of θ_{rp1} and θ_{rp2} on RT_{avg} (N_{sg}=2, p_{cuf}=60W, p_{cua}=60W, BLAC, i_d=0).

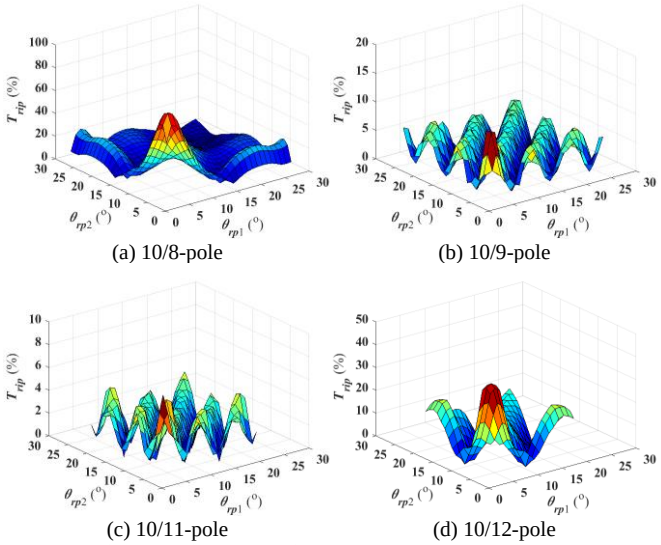

(a) 10/8-pole (b) 10/9-pole

(c) 10/11-pole (d) 10/12-pole

Fig. 15. Influence of θ_{rp1} and θ_{rp2} on T_{rip} (N_{sg}=2, p_{cuf}=60W, p_{cua}=60W, BLAC, i_d=0).

Moreover, as shown in Fig. 20, by applying the 3-segment axial pairing and selecting θ_{rp1}=8°, θ_{rp2}=17° and θ_{rp3}=18° can further suppress the peak-to-peak value of on-load induced voltage pulsation in DC winding in the 10/8-pole WFSF machine to 46.89%. Meanwhile, the average electromagnetic torque T_{avg} is reduced to RT_{avg}=90.99%, whilst the torque ripple T_{rip} can also be suppressed from 11.43% to 2.93%.

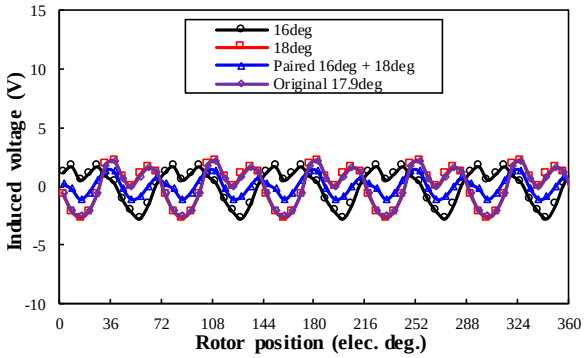

Fig. 16. On-load induced voltage pulsation in DC winding in 10/8-pole machine @ 400rpm (N_{sg}=2, p_{cuf}=60W, p_{cua}=60W, BLAC, i_d=0).

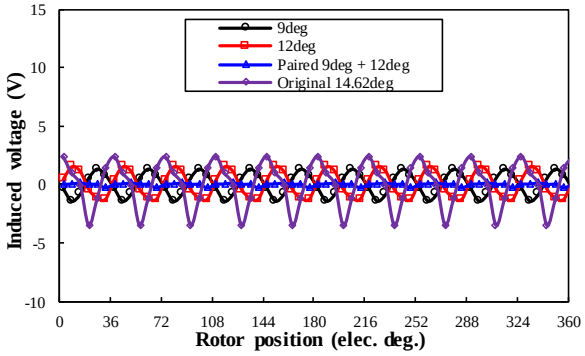

Fig. 17. On-load induced voltage pulsation in DC windings in 10/9-pole machine @ 400rpm (N_{sg}=2, p_{cuf}=60W, p_{cua}=60W, BLAC, i_d=0).

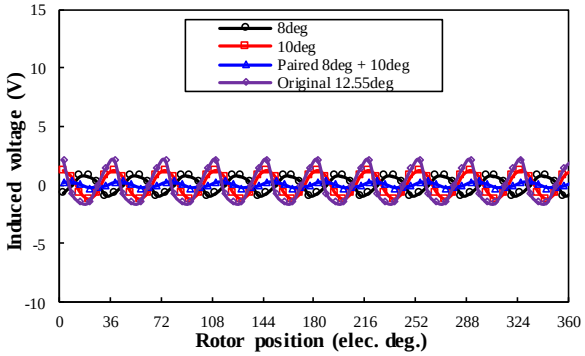

Fig. 18. On-load induced voltage pulsation in DC windings in the 10/11-pole machine @ 400rpm (N_{sg}=2, p_{cuf}=60W, p_{cua}=60W, BLAC, i_d=0).

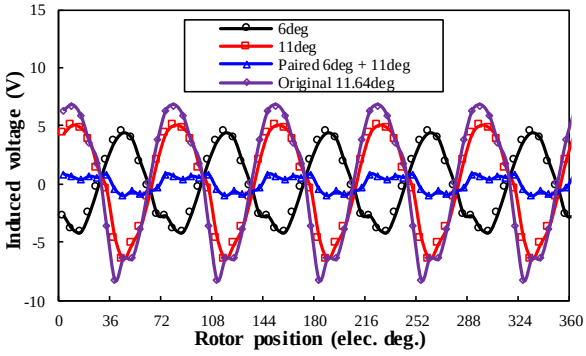

Fig. 19. On-load induced voltage pulsation in DC windings in 10/12-pole machine @ 400rpm (N_{sg}=2, p_{cuf}=60W, p_{cua}=60W, BLAC, i_d=0).

As shown in TABLE VII, by applying the rotor pole arc axial pairing, the efficiency η can be maintained as 41.24%, 43.48%, 45.98% and 44.73% for the analyzed five-phase 10/8-pole, 10/9-pole, 10/11-pole and 10/12-pole WFSF

machines, respectively. As for the 10/8-pole WFSF machine with 2-segment axial pairing and selecting (θ_{rp1}, θ_{rp2}) as (16°, 18°), η can be maintained as 43.27%. The efficiency reduction is again due to the reduced average electromagnetic torque T_{avg} in the WFSF machines with axially paired rotors, as shown in TABLE X.

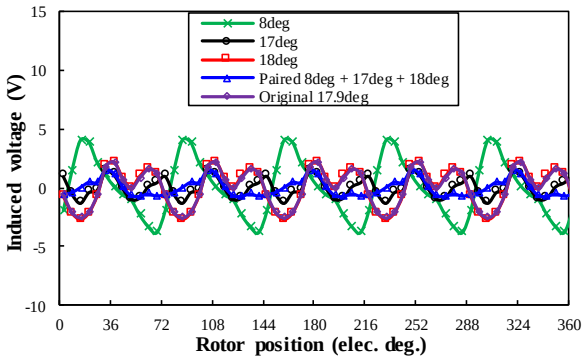

Fig. 20. On-load induced voltage pulsation in DC windings in 10/8-pole machine @ 400rpm (N_{sg}=3, p_{cuf}=60W, p_{cua}=60W, BLAC, i_d=0).

TABLE X
LOSSES AND EFFICIENCY OF FIVE-PHASE WFSF MACHINES WITH PAIRED ROTOR AT 400RPM

Items	Unit	10/8	10/9	10/11	10/12
Iron loss, p_{fe}	W	2.21*	2.13	3.13	3.79
Total copper loss, p_{cu}	W	156.72*	156.80	156.64	156.49
Electromagnetic torque, T_{em}	Nm	2.72*	2.97	3.32	3.19
Efficiency, η	%	41.24*	43.48	45.98	44.73

*: These values are based on 3-segment axial pairing. As for 2-segment axial pairing, p_{fe}=2.39W, p_{cu}=156.72W, T_{em}=2.95Nm and η=43.27%, respectively.

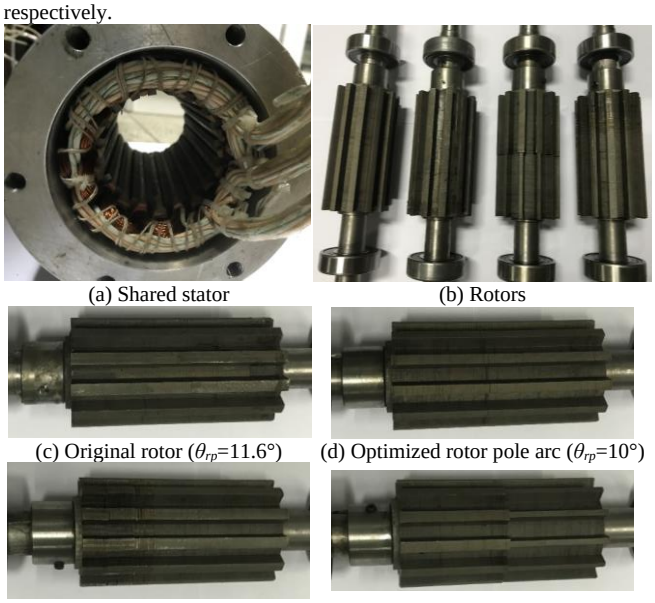

(a) Shared stator (b) Rotors

(c) Original rotor (θ_{rp}=11.6°) (d) Optimized rotor pole arc (θ_{rp}=10°)

(e) Chamfered rotor ($d_{OO'}$=15mm) (f) Paired rotor (θ_{rp1}=6°, θ_{rp2}=11°)

Fig. 21. Photos of the 10-stator-pole/12-rotor-pole WFSF prototypes.

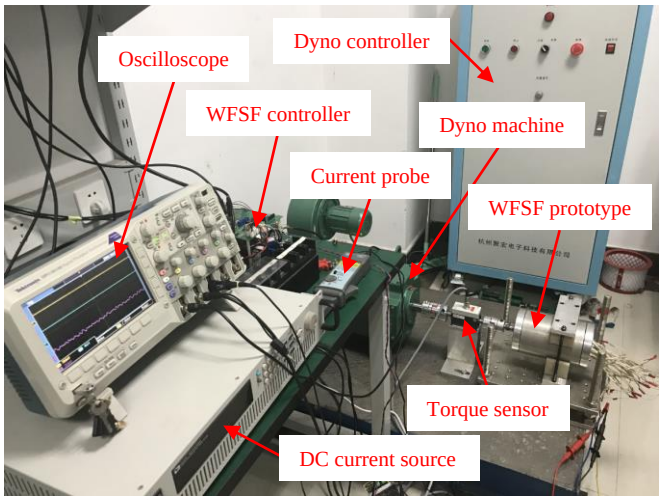

Fig. 22. Photo of the test rig.

VI. EXPERIMENTAL VALIDATION

Four WFSF machines with 10/12-stator/rotor-pole are built having the same stator which is shown in Fig. 21(a) and four different rotors which are shown in Fig. 21(b) and tested to validate the analytical results and FE predicted results. Fig. 21(c)-(f) show the original rotor with θ_{rp}=11.6°, the rotor with an optimized rotor pole arc θ_{rp}=10°, the chamfered rotor with $d_{OO'}$=15mm, the rotor with two axial paired segments having θ_{rp1}=6° and θ_{rp2}=11°, respectively. Based on the test rig shown in Fig. 22, electromagnetic performance under both open-circuit and on-load conditions are tested and given as follows. To validate the FE predicted open-circuit AC winding back-EMF and on-load DC winding induced voltage under a constant DC winding current, in this section the DC winding is excited by a constant DC current source, as shown in Fig. 22.

A. *Open-circuit AC Winding Back EMF*

Fig. 23(a) shows the comparison of the FE predicted and measured open-circuit A- and B-phase back EMF waveforms of the prototype having the original rotor, together with the measured DC winding current and voltage. Similar waveforms of Fig. 23(b)-Fig. 23(d) are for the prototypes having three modified rotors, respectively. As shown in Fig. 23, for all four prototypes, the measured A-phase open-circuit back EMF agrees well with the FE predicted results.

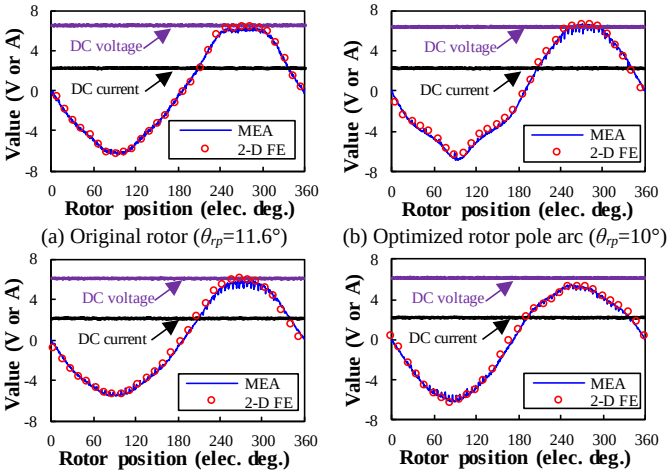

(a) Original rotor (θ_{rp}=11.6°) (b) Optimized rotor pole arc (θ_{rp}=10°)

(c) Chamfered rotor ($d_{OO'}$=15mm) (d) Paired rotor (θ_{rp1}=6°, θ_{rp2}=11°)

Fig. 23. Comparison of FE predicted and measured A-phase back EMF together with the measured DC winding current and voltage.

B. *On-Load Induced Voltage Pulsation in DC Winding*

Here, the prototypes operate in generator condition, not motor condition, with pure resistance load 1.8Ω for each phase. This is to exempt the induced voltage pulsation in DC winding component caused by high frequency current pulse width modulation (PWM) harmonics in AC windings, as shown in Appendix C.

Fig. 24(a) illustrates the comparison between the FE predicted and measured on-load induced voltage for DC coil 2 of the prototype having the original rotor, together with A-phase winding current and DC winding current. Fig. 24(b)-Fig. 24(d) show these characteristics of the prototypes having three modified rotors, respectively. Here, DC coils 2, 4, 6, 8, and 10 are open-circuited, and only the on-load induced voltage pulsation in DC coil 2 is measured, not the complete induced voltage pulsation in DC winding, as the impact of the DC power supply on the induced voltage pulsation in DC winding cannot be separated [47]. However, a doubled current is injected into DC coils 1, 3, 5, 7 and 9, to produce the same DC winding MMF. In the 10/12-pole WFSF machine, the phase shift of the on-load DC winding induced voltage waveforms for every two adjacent DC coils is 72 electric degrees, thus the DC winding induced voltage of other nine DC coils and that of the whole DC winding can be obtained based on the DC coil 2 induced voltage pulsation.

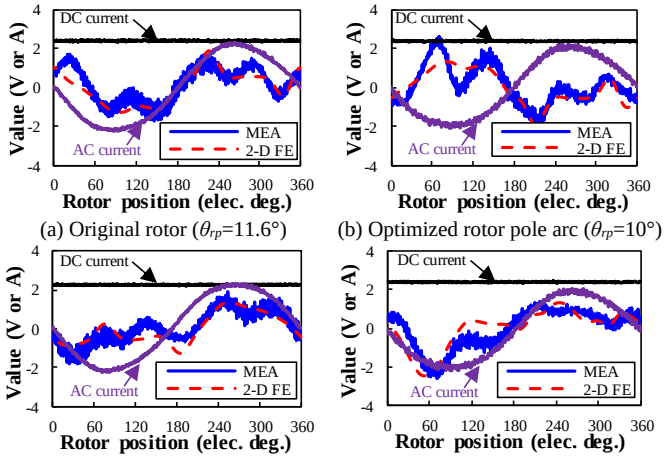

(a) Original rotor (θ_{rp}=11.6°) (b) Optimized rotor pole arc (θ_{rp}=10°)

(c) Chamfered rotor ($d_{OO'}$=15mm) (d) Paired rotor (θ_{rp1}=6°, θ_{rp2}=11°)

Fig. 24. Variation of FE predicted and measured DC coil 2 induced voltages together with the measured A-phase winding current and DC winding current.

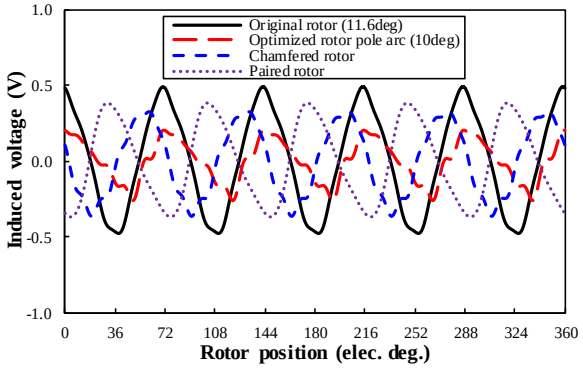

(a) Waveforms

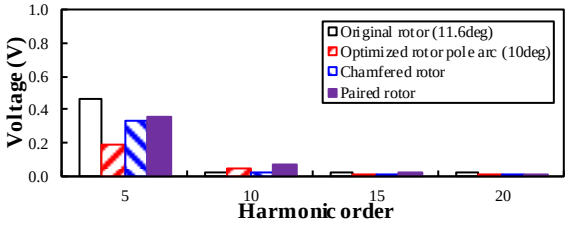

(b) Spectra

Fig. 25. On-load induced voltage pulsation in DC winding.

As shown in Fig. 24, the measured DC coil 2 on-load induced voltage again agrees well with the FE predicted results in all four prototypes, respectively. The measured waveforms are slightly distorted, which is also caused by imperfect manufacturing. Moreover, based on the measured DC coil 2 on-load induced voltage waveforms shown in Fig. 24, induced voltage pulsation in DC winding can be obtained as shown in Fig. 25. As shown in Fig. 25(a), the on-load DC winding induced voltage peak-to-peak value E_{pp} can be suppressed to 47.95%, 71.23% and 77.69% by applying the rotor pole arc optimization, rotor pole chamfering and rotor pole arc axial pairing, respectively. As forging analyzed, only the 5k (k=1,2,3,…) harmonics of the induced voltage of DC coil 2 will be tenfold in the DC winding induced voltage as there are ten DC coils, whilst other harmonics will be cancelled. It can be found from Fig. 25(b) that the dominant 5th harmonic in the original machine can be suppressed to 40.12%, 70.88% and 77.67% in the modified machines with optimized pole arc rotor, chamfered rotor and paired rotor, respectively. The experimental suppression of on-load DC winding induced voltage by applying rotor pole chamfering and rotor pole arc axial pairing is not substantial. This is mainly caused by the distorted DC coil 2 induced voltage waveform shown in Fig. 24, due to imperfect manufacturing.

The shaft torques of four prototypes under generator condition with pure resistance load 1.8Ω for each phase are shown in Fig. 26, when the DC winding current I_f=2.2A and the DC winding voltage is U_f=6.3V. As shown in TABLE XI, the measured average torques agree well with the 2-D FE predicted values for all four prototypes.

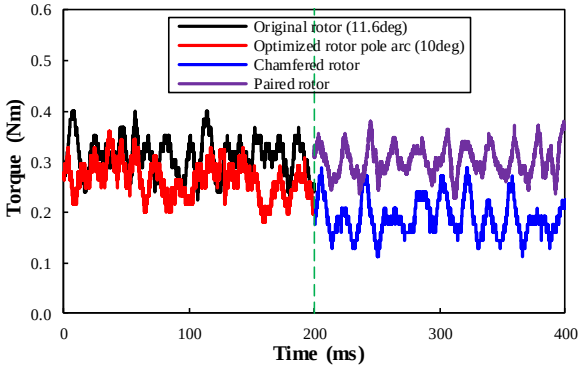

Fig. 26. On-load measured shaft torques at 400rpm in generator condition with pure resistance load 1.8Ω per phase (I_f=2.2A, U_f=6.3V).

TABLE XI
COMPARISON OF MEASURED AND 2-D FE PREDICTED ELECTROMAGNETIC TORQUE @400RPM (UNIT: NM)

Mode	Rotor	Original	Optimized	Chamfered	Paired
Generator	Measured	0.31	0.27	0.19	0.30
	2-D FE	0.29	0.27	0.19	0.32
Motor	Measured	N/A	3.03	2.79	2.73
	2-D FE	3.15	3.10	2.91	2.89

The shaft torques of three modified prototypes under motor condition are shown in Fig. 26, when I_f=2.2A and U_f=6.3V. All three modified prototypes operate at BLAC mode with i_d=0 and i_q=9A. Again, the measured average

torques agree well with the 2-D FE predicted values for all three prototypes, as shown in TABLE XI.

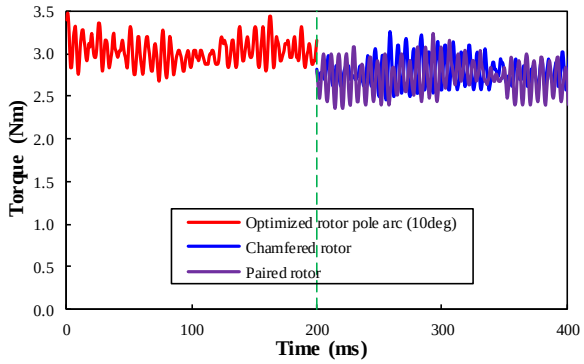

Fig. 27. On-load measured shaft torques at 400rpm in motor condition (I_f=2.2A, U_f=6.3V, BLAC, i_d=0, i_q=9A).

VII. Conclusions

Induced voltage pulsation in DC winding of five-phase WFSF machines is analyzed together with some suppression methods proposed in this paper. Analytical model shows that the open-circuit and armature reaction induced voltage pulsation in DC winding cycles per electric period N_{peopen} and N_{pearma} for the N_s-stator-pole/N_r-rotor-pole WFSF machines are $LCM(N_s, N_r)/N_r$, where LCM is the largest common multiplier, and 5r (r=1 or 2 for machines having zero or non-zero even-order harmonic winding factors, respectively), respectively. Modifying the airgap permeance, i.e. optimizing the rotor pole arc or shaping the rotor pole surface, and axial pairing of rotor segments with different rotor pole arcs can effectively suppress the induced voltage pulsation in DC winding, with >90% average electromagnetic torque being maintained.

Appendix A

In this Appendix, the dimensional parameters of the five-phase 10/12-stator/rotor-pole WFSF machine and the three-phase 12/10-stator/rotor-pole WFSF machine listed in TABLE I are shown in TABLE XII. In TABLE XII, $d_{OO'}$ is the rotor pole surface center displacement due to chamfering, which can be referred in Fig. 9. The definitions of other symbols in TABLE XII are the same as those in TABLE II. They are obtained from two steps. Firstly, the main dimensional parameters are globally optimized for the largest average electromagnetic torque by genetic algorithm using ANSYS Maxwell, under brushless AC (BLAC) condition with zero d-axis current control, i.e. i_d=0, due to a negligible reluctance torque [25], [26]. Then, to reduce the torque ripple, the rotor pole is chamfered [56] to modify the equivalent airgap length and hence the airgap permeance. The rotor pole surface center displacement $d_{OO'}$ is optimized to achieve the lowest torque ripple T_{rip} with the criterion that T_{avg}≥205Nm.

TABLE XII
Main Dimensional Parameters of Five-Phase 10/12-Pole and Three-Phase 12/10-Pole WFSF Machines

Parameters	R_{sy} (mm)	R_{si} (mm)	R_{ry} (mm)	θ_{st} (°)	θ_{ssdc} (°)	θ_{rp} (°)	$d_{OO'}$ (mm)
Five-phase 10/12-pole	121.7	86.64	71.94	6.49	12.17	11.45	68
Three-phase 12/10-pole	121.7	89.2	67.54	5.37	9.50	11.79	46

As shown in Fig. 28, after chamfering, the torque ripple T_{rip} of the five-phase WFSF machine can be suppressed from 40.53% to 1.43%, whilst the average torque T_{avg} reduced by 9.46% from 266.4Nm to 241.2Nm. As for the three-phase WFSF machine, the torque ripple T_{rip} can be reduced from 16.95% to 7.26%, whilst the average torque T_{avg} will be reduced by 7.30% from 221.3Nm to 205.2Nm. Here, it is worth noting that the rotor of the Toyota Prius 2010 IPM machine is also shaped [47],[48], which can reduce the torque ripple from 19.70% to 9.96%, in spite of a 1.5% reduction of average electromagnetic torque from 209.2Nm to 206.1Nm, as shown in Fig. 28.

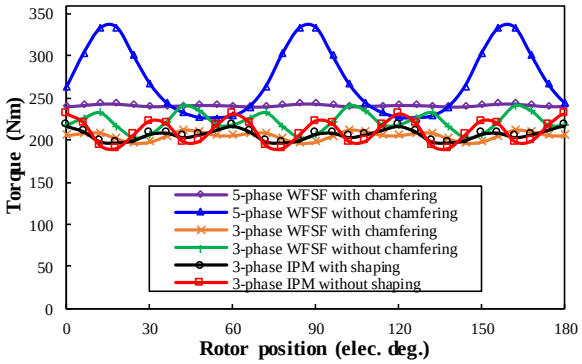

Fig. 28. Rated on-load torque waveforms in the 5-phase WFSF machine, 3-phase WFSF machine and the Toyota Prius 2010 IPM machine (BLAC, J_s=26.8A/mm^2).

Appendix B

In this Appendix, the analysis with the criteria accounting both the average electromagnetic torque T_{avg} and the torque ripple T_{rip} by adopting the techniques to reduce the on-load DC winding induced voltage is discussed. Here, the criterion for T_{avg} remains the same, i.e. RT_{avg}>90%, whilst the torque ripple T_{rip} should not be 10% higher than the original machine. As for other criteria with different values of RT_{avg} and the change of T_{rip}, similar analysis can be applied.

A. Rotor Pole Arc Optimization

By applying the rotor pole arc optimization, the optimal rotor pole arc is θ_{rpopt}=17°, 14° and 11° for the 10/9-, 10/11- and 10/12-pole WFSF machines, as shown in Fig. 7 and TABLE XIII. However, there is no available θ_{rpopt} for the 10/8-pole WFSF machine, since the torque ripple T_{rip} of the original design is very low. This means the criterion for T_{rip} needs to be modified.

TABLE XIII
Characteristics of Modified WFSF Machines with Both RT_{avg} and T_{rip} Accounted @400rpm

Technique	Item	Unit	10-stator-pole WFSF machines			
-	N_r	-	8	9	11	12
θ_{rp} optimization	RT_{avg}	%	-	93.18	98.19	99.12
	T_{rip}	%	-	5.14	3.12	15.09
	RE_{pp}	%	-	30.67	48.39	76.59
Chamfering	RT_{avg}	%	95.64	93.45	97.46	92.07
	T_{rip}	%	6.78	3.00	2.68	6.97
	RE_{pp}	%	61.76	45.47	93.62	40.21
Pairing	RT_{avg}	%	90.99*	90.65	93.55	90.82
	T_{rip}	%	2.93	2.34	2.41	7.18
	RE_{pp}	%	46.89*	7.16	15.64	12.04

*: These two values are based on 3-segment axial pairing. As for 2-segment axial pairing, RT_{avg}=99.06%, T_{rip}=12.19% and RE_{pp}=52.65%, respectively.

B. Rotor Pole Chamfering

By applying the rotor pole chamfering, the optimal displacement $d_{OO'}$ are 6mm, 11mm, 7mm and 15mm for the 10/8-, 10/9-, 10/11- and 10/12-pole WFSF machines, respectively. The optimal $d_{OO'}$ are the same as those under only the criterion with RT_{avg}>90%, since the rotor pole

chamfering can also reduce torque ripple, as shown in Fig. 10.

C. Rotor Pole Arc Axial Pairing

By applying the rotor pole arc pairing, again the results are the same as those under the criterion with only RT_{avg}>90%, as shown in TABLE XIII.

APPENDIX C

The AC winding current harmonics caused by PWM also generate additional armature reaction flux-linkage in all DC coils. For example, the additional armature reaction flux-linkage in DC coil 1 ψ_{1pwmA} due to A-phase winding current harmonics caused by PWM can be given by,

$$\psi_{1pwmA}(\theta_e) = M_{1A}(\theta_e) \times I_{pwm} \cos\left(\frac{f_{pwm}}{f_e}\theta_e + \beta_{pwm}\right) \quad (28)$$

where M_{1A} is the mutual inductances between the DC coil 1 and the A-phase winding. I_{pwm} is the amplitude of the A-phase current harmonic caused by PWM. f_{pwm} is the switching frequency of the power semiconductor device driven by PWM, e.g. 10kHz. f_e is the electric frequency of the AC fundamental currents. β_{pwm} is the initial phase of A-phase current harmonic due to PWM. Here, other higher order harmonics caused by PWM are not considered.

Based on (28), the additional armature reaction induced voltage in DC coil 1 v_{1pwmA} due to A-phase winding current harmonics caused by PWM can be given by,

$$\begin{aligned} v_{1pwmA}(\theta_e) &= \frac{d\psi_{1pwmA}}{dt} = \\ &= I_{pwm}\omega_e \frac{dM_{1A}(\theta_e)}{d\theta_e} \times \cos\left(\frac{f_{pwm}}{f_e}\theta_e + \beta_{pwm}\right) \\ &- \frac{I_{pwm}f_{pwm}\omega_e}{f_e} M_{1A}(\theta_e) \times \sin\left(\frac{f_{pwm}}{f_e}\theta_e + \beta_{pwm}\right) \end{aligned} \quad (29)$$

Although the amplitude of the current harmonic I_{pwm} caused by PWM in (29) is much lower than the AC phase fundamental currents, the switching frequency f_{pwm} is much higher than the electric frequency of the AC fundamental currents, e.g. 125 times for f_{pwm}=10kHz and f_e=80Hz for the 10/12-pole WFSF prototype at 400rpm. This makes the second item of v_{1pwmA} in (29) cannot be neglected.

ACKNOWLEDGEMENT

The authors would like to thank Prof. Kai Wang and Mr. Han Zhang from Nanjing University of Aeronautics and Astronautics for their help in experiments.

REFERENCES

[1] Z. Q. Zhu and D. Howe, "Electrical machines and drives for electric, hybrid and fuel cell vehicles," *Proc. IEEE*, vol. 95, no. 4, pp. 746–765, Apr. 2007.

[2] J. Cros and P. Viarouge, "Synthesis of high performance PM motors with concentrated windings," *IEEE Trans. Energy Convers.*, vol. 17, no. 2, pp. 248–253, Jun. 2002.

[3] T. M. Jahns, G. B. Kliman, and T. W. Neumann, "Interior permanent-magnet synchronous motors for adjustable-speed drives," *IEEE Trans. Ind. Appl.*, vol. IA–22, no. 4, pp. 738–747, Jul. 1986.

[4] M. Cheng, W. Hua, J. Zhang, and W. Zhao, "Overview of stator-permanent magnet brushless machines," *IEEE Trans. Ind. Electron.*, vol. 58, no. 11, pp. 5087–5101, Nov. 2011.

[5] A. M. El-Refaie, T. M. Jahns, and D. W. Novotny, "Analysis of surface permanent magnet machines with fractional-slot concentrated windings," *IEEE Trans. Energy Convers.*, vol. 21, no. 1, pp. 34–43, Mar. 2006.

[6] K. T. Chau, C. C. Chan, and C. Liu, "Overview of permanent-magnet brushless drives for electric and hybrid electric vehicles," *IEEE Trans. Ind. Electron.*, vol. 55, no. 6, pp. 2246–2257, Jun. 2008.

[7] K. Wang, J. Li, S. S. Zhu, and C. Liu, "Novel hybrid-pole rotors for consequent-pole PM machines without unipolar leakage flux," *IEEE Trans. Ind. Electron.*, vol. 66, no. 9, pp. 302-309, Jan. 2019.

[8] I. Boldea, L. N. Tutelea, L. Parsa, and D. Dorrell, "Automotive electric propulsion systems with reduced or no permanent magnets: an overview," *IEEE Trans. Ind. Electron.*, vol. 61, no. 10, pp. 5696–5711, Oct. 2014.

[9] E. Sulaiman, T. Kosaka, and N. Matsui, "Design study and experimental analysis of wound field flux switching motor for HEV applications," in *Proc. IEEE Inter. Conf. Elec. Mach.*, Marseille, France, Sep. 2012, pp. 1269–1275.

[10] E. Sulaiman, T. Kosaka, and N. Matsui, "A new structure of 12slot-10pole field-excitation flux switching synchronous machine for hybrid electric vehicles," in *Proc. 14th Eur. Conf. Power Electron. Appl.*, Birmingham, UK, Aug.-Sep. 2011, pp. 1–10, paper 245.

[11] T. Raminosoa, A. M. El-Refaie, D. Pan, K. K. Huh, J. P. Alexander, K. Grace, S. Grubic, S. Galioto, P. B. Reddy, and X. Shen, "Reduced rare-earth flux-switching machines for traction applications," *IEEE Trans. Ind. Appl.*, vol. 51, no. 4, pp. 2959–2971, Jul.-Aug. 2015.

[12] T. Raminosoa, D. Torrey, A. M. El-Refaie, K. Grace, D. Pan, S. Grubic, K. Bodla, and K.-K. Huhet, "Sinusoidal reluctance machine with DC winding: an attractive non-permanent-magnet option," *IEEE Trans. Ind. Appl.*, vol. 52, no. 3, pp. 2129–2137, May/Jun. 2016.

[13] M. L. Bash and S. D. Pekarek, "Modeling of salient-pole wound-rotor synchronous machines for population-based design," *IEEE Trans. Energy Convers*., vol. 26, no. 2, pp. 381–392, Jun. 2011.

[14] E. Levi, "A unified approach to main flux saturation modelling in D-Q axis models of induction machines," *IEEE Trans. Energy Convers*., vol. 10, no. 3, pp. 455–461, Sep. 1995.

[15] B. Fahimi, A. Emadi, and R. B. Sepe, "A switched reluctance machine-based starter/alternator for more electric cars," *IEEE Trans. Energy Convers*., vol. 19, no. 1, pp. 116–124, Mar. 2004.

[16] A. Chiba, Y. Takano, M. Takeno, T. Imakawa, N. Hoshi, M. Takemoto, and S. Ogasawara, "Torque density and efficiency improvements of a switched reluctance motor without rare-earth material for hybrid vehicles," *IEEE Trans. Ind. Appl*., vol. 47, no. 3, pp. 1240–1246, May/Jun. 2011.

[17] T. Matsuo and T. A. Lipo, "Rotor design optimization of synchronous reluctance machine," *IEEE Trans. Energy Convers*., vol. 9, no. 2, pp. 359–365, Jun. 1994.

[18] Y. Fan, K. T. Chau, and S. Niu, "Development of a new brushless doubly fed doubly salient machine for wind power generation," *IEEE Trans. Magn.*, vol. 42, no. 2, pp. 3455–3457, Oct. 2006.

[19] R. Cao, X. Yuan, Y. Jin, and Z. Zhang, "MW-class stator wound field flux-switching motor for semidirect drive wind power generation system," *IEEE Trans. Ind. Electron.*, vol. vol. 66, no. 1, pp. 795–805, Jan. 2019.

[20] U. B. Akuru and M. J. Kamper, "Formulation and multiobjective design optimization of wound-field flux switching machines for wind energy drives," *IEEE Trans. Ind. Electron.*, vol. 65, no. 2, pp. 1828–1836, Feb. 2018.

[21] X. Li, S. Yu, and Y. Wang, "A novel HTS claw-pole vernier machine using single excitation unit with stationary seal," *IEEE Trans. Appl. Supercond.*, vol. 29, no. 5, Art no. 5201505, Aug. 2019.

[22] X. Li, X. Wang, and Y. Wang, "Design and analysis of a new HTS linear flux-controllable doubly salient machine," *IEEE Trans. Appl. Supercond.*, vol. 29, no. 5, Art no. 5201605, Aug. 2019.

[23] C. Pollock and M. Wallace, "The flux switching motor, a DC motor without magnets or brushes," in *Conf. Rec. IEEE IAS Annu. Meeting*, 1999, vol. 3, pp. 1980–1987.

[24] J. T. Chen, Z. Q. Zhu, S. Iwasaki, and R. Deodhar, "Low cost flux-switching brushless AC machines," in *Proc. Veh. Pow. Prop. Conf*., Lille, France, 2010, pp. 1–6.

[25] Z. Q. Zhu and X. Liu, "Novel stator electrically field excited synchronous machines without rare-earth magnet," *IEEE Trans. Magn.*, vol. 51, no. 4, Apr. 2015, Art. ID 8103609.

[26] Z. Q. Zhu and Y. J. Zhou, "Recent development in stator wound field synchronous machines", *Chinese Journal of Electrical Engineering*, vol. 10, no. 4, pp.11–25, Apr. 2015.

[27] C. H. T. Lee, K. T. Chau, C. Liu, and C. C. Chan, "Overview of magnetless brushless machines," *IET Elec. Power Appl.*, vol. 12, no. 8, pp. 1117–1125, Sep. 2018.

[28] A. Zulu, B. Mecrow, and A. Armstrong, "A wound-field three-phase flux switching synchronous motor with all excitation sources on the stator," *IEEE Trans. Ind. Appl.*, vol. 46, no. 6. pp. 2363–2371, Nov.-Dec. 2010.

[29] F. Khan, E. Sulaiman, and M. Z. Ahmad, "Coil test analysis of wound-field three-phase flux switching machine with non-overlapping winding and salient rotor," *in Proc. IEEE 8th Int. Power Eng. Optim. Conf.*, Langkawi, Malaysia, Mar. 2014, pp. 243–247.

[30] Z. Q. Zhu, Y. J. Zhou, J. T. Chen and J. E. Green, "Investigation of nonoverlapping stator wound-field synchronous machines," *IEEE Trans. Energy Convers.*, vol. 30, no. 4, pp. 1420–1427, Dec. 2015.
[31] T. Fukami, Y. Matsuura, K. Shima, M. Momiyama, and M. Kawamura, "Development of a low-speed multi-pole synchronous machine with a field winding on the stator side," in *Proc. Int. Conf. Elec. Mach.*, Rome, Italy, 2010, pp. 1–6.
[32] T. Fukami, Y. Matsuura, K. Shima, M. Momiyama, and M. Kawamura, "A multi-pole synchronous machine with nonoverlapping concentrated armature and field winding on the stator," *IEEE Trans. Ind. Electron.*, vol. 59, no. 6, pp. 2583–2591, Jun. 2012.
[33] Y. Kashitani and S. Shimomura, "Novel slipring-less winding-excited synchronous machine," in *Int. Conf. Elect. Mach. and Syst*., Beijing, China, Sep. 2012, pp. 1–6.
[34] T. Fukami, K. Shima, T. Tsuda, and M. Kawamura, "Prediction of field currents in flux-modulating synchronous machines under loaded conditions," in *Proc. Int. Conf. Elec. Mach.*, Marseille, France, 2012, pp. 441–446.
[35] X. Liu and Z. Q. Zhu, "Stator/rotor pole combinations and winding configurations of variable flux reluctance machines", *IEEE Trans. Ind. Appl.*, vol. 50, no. 6, pp.3675–3684, Nov. 2014.
[36] L. Xu, G. Liu, W. Zhao, J. Ji, H. Zhou, and T. Jiang, "Design and analysis of a new linear wound-field flux reversal machine based on magnetic gear effect," *IEEE Trans. Magn.*, vol. 51, no. 11, Nov. 2015, Art. ID 15552880.
[37] Z. Zhang, Y. Yan, and Y. Tao, "A new topology of low speed doubly salient brushless DC generator for wind power generation," *IEEE Trans. Magn.*, vol. 48, no. 3, pp. 1227–1233, Mar. 2012.
[38] Z. Zhang, L. Yu, C. Dai, and Y. Yan, "Investigation and development of a new brushless DC generator system for extended-range electric vehicle application," in *Proc. IEEE Energy Convers. Congr. Expo.*, Pittsburgh, PA, USA, Sep. 2014, 3155–3162.
[39] Z. Zhang, L. Yu, L. Sun, L. Qian, and X. Huang, "Iron loss analysis of doubly salient brushless DC generators," *IEEE Trans. Ind. Electron.*, vol. 62, no. 4, pp. 2156–2163, Apr. 2015.
[40] W. Hua, P. Su, M. Tong, and J. Meng, "Investigation of a five-phase E-core hybrid-excitation flux-switching machine for EV and HEV applications," *IEEE Trans. Ind. Appl.*, vol. 53, no. 1, pp. 124–133, Jan./Feb. 2017.
[41] W. Zhao, C. Gu, Q. Chen, J. Ji, and D. Xu, "Remedial phase-angle control of a five-phase fault-tolerant permanent-magnet vernier machine with short-circuit fault," *CES Trans. Elec. Mach. and Syst.*, vol. 1, no. 1, pp. 83–88, Mar. 2017.
[42] X. Xue, W. Zhao, J. Zhu, G. Liu, X. Zhu, and M. Cheng, "Design of five-phase modular flux-switching permanent-magnet machines for high reliability applications," *IEEE Trans. Magn.*, vol. 49, no. 7, pp. 3941–3944, Jul. 2013.
[43] J. Luo, W. Zhao, J. Ji, J. Zheng, Y. Zhang, Z. Ling, and J. Mao, "Reduction of eddy-current loss in flux-switching permanent-magnet machines using rotor magnetic flux barriers," *IEEE Trans. Magn.*, vol. 53, no. 11, Nov. 2017, Art. ID 17284159.
[44] K. Wang, Z. Y. Gu, Z. Q. Zhu, and C. Liu, "Design and analysis of five phase SPM machine considering third harmonic current injection," *IEEE Trans. Energy Convers.*, vol. 33, no. 3, pp. 1108–1117, Sept. 2018.
[45] K. Wang, Z. Y. Gu, Z. Q. Zhu, and Z. Z. Wu, "Optimum injected harmonics into magnet shape in multi-phase surface-mounted PM machine for maximum output torque," *IEEE Trans. Ind. Electron.*, vol. 64, no. 6, pp. 4434-4443, 2017.
[46] K. Wang, Z. Q. Zhu, Y. Ren, and G. Ombach, "Torque improvement of dual three-phase permanent magnet machine with 3rd harmonic current injection," *IEEE Trans. Ind. Electron.*,, vol. 62, no. 11, pp. 6833-6844, Nov. 2015.
[47] T. A. Burress *et al.*, "Evaluation of the 2010 Toyota Prius hybrid synergy drive system," Oak Ridge Nat. Lab., Oak Ridge, TN, USA, Rep. ORNL/TM2010/253, 2011.
[48] Y. Guan, Z. Q. Zhu, I. A. A. Afinowi, J. C. Mipo and P. Farah, "Design of synchronous reluctance and permanent magnet synchronous reluctance machines for electric vehicle application," in *Int. Conf. Elect. Mach. and Syst*., Hangzhou, China, Oct. 2014, pp. 1853–1859.
[49] Z. Z. Wu, Z. Q. Zhu, C. Wang, J. Mipo, S. Personnaz, and P. Farah, "Influence of DC winding configuration on its induced voltage in wound field machines," *IEEE Trans. Energy Convers.*, vol. 33, no. 4, pp. 1825–1836, Dec. 2018.
[50] Z. Wu, Z. Q. Zhu, C. Wang, J. Mipo, S. Personnaz, and P. Farah, "Reduction of open-circuit DC winding induced voltage in wound field switched flux machines by skewing," *IEEE Trans. Ind. Electron.*, vol. 66, no. 3, pp. 1715–1726, Mar. 2019.
[51] Z. Z. Wu and Z. Q. Zhu, "Analysis of air-gap field modulation and magnetic gearing effects in switched flux permanent magnet machines," *IEEE Trans. Magn.*, vol. 51, no. 5, May 2015, Art. ID 15143861.
[52] S. Jia, R. Qu, J. Li, and D. Li, "Principles of stator dc winding excited vernier reluctance machines," *IEEE Trans. Energy Convers.*, vol. 31, no. 3, pp. 935–946, Sep. 2016.
[53] M. Cheng, P. Han, and W. Hua, "General airgap field modulation theory for electrical machines," *IEEE Trans. Ind. Electron.*, vol. 64, no. 8, pp. 6063–6074, Aug. 2017.
[54] S. Chen, *Electrical Machine Design*. Beijing, China: MI Press, 1990.
[55] W. Hua, M. Cheng, Z. Q. Zhu, and D. Howe, "Analysis and optimization of back EMF waveform of a flux-switching permanent magnet motor," *IEEE Trans. Energy Convers.*, vol. 23, no. 3, pp. 727–733, Sep. 2008.
[56] M. J. Jin, Y. Wang, J. X. Shen, P. C. K. Luk, W. Z. Fei, and C. F. Wang, "Cogging torque suppression in a permanent-magnet flux-switching integrated-starter-generator," *IET Elec. Power Appl.*, vol. 4, no. 8, pp. 647–656, Sep. 2010.
[57] Y. Wang, M. J. Jin, W. Z. Fei, and J. X. Shen, "Cogging torque reduction in permanent magnet flux-switching machines by rotor teeth axial pairing," *IET Elec. Power Appl.*, vol. 4, no. 7, pp. 500–506, Aug. 2010.

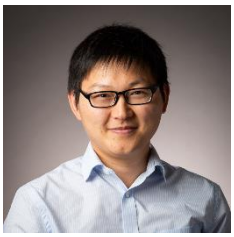

Z. Z. Wu (S'15-M'18) received the B.Eng. and M.Sc. degrees in electrical engineering from Southeast University, Nanjing, China, in 2010 and 2013, respectively, and the Ph.D. degree in electrical and electronic engineering from The University of Sheffield, Sheffield, U.K., in January 2017.

Since August 2018, he has been with Powertrain and Vehicle Research Centre, Department of Mechanical Engineering, University of Bath, Bath, U.K., where he is currently a Prize Fellow in Electric Propulsion. His major research interests include the advanced electrical machines and drives for electric propulsion systems.

From January 2017 to August 2018, he was with Warwick Manufacturing Group (WMG), University of Warwick, Coventry, U.K., as a research fellow in electrical machines.

Z. Q. Zhu (M'90–SM'00–F'09) received the B.Eng. and M.Sc. degrees in electrical and electronic engineering from Zhejiang University, Hangzhou, China, in 1982 and 1984, respectively, and the Ph.D. degree in electrical and electronic engineering from The University of Sheffield, Sheffield, U.K., in 1991.

Since 1988, he has been with The University of Sheffield, where he is currently a Research Chair of the Royal Academy of Engineering/Siemens with the Department of Electronic and Electrical Engineering and the Head of the Electrical Machines and Drives Research Group. His current research interests include the design and control of permanent-magnet brushless machines and drives for applications ranging from automotive through domestic appliances to renewable energy.

Dr. Zhu is a Fellow of the Royal Academy of Engineering.

Wei Hua (M'03-SM'16) received B.Sc. and Ph.D. degrees both in Electrical Engineering from the School of Electrical Engineering, Southeast University, Nanjing, China, in 2001 and 2007, respectively. During 2004.9-2005.8, he visited the department of Electronics and Electrical Engineering, The University of Sheffield, UK as a joint-supervised Ph. D. student.

Since 2007, he has been with Southeast University, where he is currently a Professor in Electrical Engineering with the School of Electrical Engineering. He is the author or coauthor of over 140 technical papers, and he is the holder of 30 patents in his areas of interest. His teaching and research interests include the design, analysis, and control of electrical machines.

Sam Akehurst received B. Eng. and Ph.D. degrees in Mechanical Engineering from Department of Mechanical Engineering, University of Bath, Bath, U.K. in 1996 and 2000, respectively.

Since 2000, he has been with University of Bath, Bath, U.K., where he is currently a Professor in Advanced Powertrain Systems with Department of Mechanical Engineering. His teaching and research interests include advanced powertrain systems and electrification.

Xiaofeng Zhu received the B.Sc. degree from the School of Electrical Engineering, Shenyang University of Technology, Shenyang, China, in 2012 and the M.Sc. degree from National Engineer Research Center for Rare Earth Permanent Magnet Machines, Shenyang University of Technology, in 2015, both in electrical engineering. Since 2015, he has been working toward the Ph.D. degree in electrical engineering in the School of Electrical Engineering, Southeast University, Nanjing, China.

His major research interests include the design, analysis and optimization of PM machines.

Jie Hu was born in Jiangxi, China, in 1995. He received the B.Eng. degree in electrical engineering and its automation from Southeast University, Nanjing, China, in July 2017. Since September 2017, he has been working toward the M.Sc. degree in the same institute.

His major research interests include the servo control of low speed permanent magnet synchronous machines.

Haoyang Li received the B.Eng. degree in electrical engineering and its automation from Southeast University, Nanjing, China, in July 2017. Since September 2017, he has been working toward the M.Sc. degree in the same institute.

His major research interests include fault tolerant control of multi-unit in-wheel motors for electric vehicles.

Junming Zhu received the B.Sc. degree in electrical engineering and its automation from Suzhou University of Science and Technology, Suzhou, China, in July 2016. Since September 2016, he has been working toward the M.Sc. degree in school of electrical engineering, Southeast University, Nanjing, China.

His research interests include design, control and parameter identification of permanent magnet synchronous machines.